First Example of Protonation of Ruddlesden–Popper Sr 2 IrO 4 : A Route to Enhanced Water Oxidation Catalysts

Ronghuang Zhang, Paul E Pearce, Vanessa Pimenta, Jordy Cabana, Heifang Li, Daniel Alves, Dalla Corte, Artem M Abakumov, Gwenaëlle Rousse, Domitille Giaume, et al.

First example of protonation of Ruddlesden-Popper Sr_2IrO_4: a route to enhanced water oxidation catalysts

Ronghuang Zhang,[1,2] Paul E. Pearce,[1,2,3] Vanessa Pimenta,[4] Jordy Cabana,[5,6,7] Heifang Li,[5,6,7] Daniel Alves Dalla Corte, [1,2] Artem M. Abakumov,[8] Gwenaëlle Rousse, [1,2,3] Domitille Giaume,[9] Michaël Deschamps,[10,11] Alexis Grimaud[1,2]*

[1]Chimie du Solide et de l'Energie, UMR 8260, Collège de France, 75231, Paris Cedex 05, France

[2]Réseau sur le Stockage Electrochimique de l'Energie (RS2E), CNRS FR 3459,33 rue Saint Leu, 80039, Amiens Cedex, France

[3]Sorbonne Université, Paris, France

[4]Institut des Matériaux Poreux de Paris, UMR 8004 CNRS, Ecole Normale Supérieure, Ecole Supérieure de Chimie et de Physique Industrielle de Paris, PSL University, 75005, Paris, France

[5]Advanced Photon Source, Argonne National Laboratory, Argonne, Illinois 60439, United States

[6]Department of Chemistry, University of Illinois at Chicago, Chicago, Illinois 60607, United States

[7]Joint Center for Energy Storage Research (JCESR), Argonne National Laboratory, Lemont, Illinois 60439, United States

[8]Skoltech Center for Energy Science and Technology, Skolkovo Institute of Science and Technology, Moscow 143026, Russia

[9]Chimie ParisTech, PSL University, CNRS, Institut de Recherche de Chimie Paris, 75005 Paris, France

[10]CNRS, CEMHTI UPR3079, Université d'Orléans, 1D avenue de la recherche scientifique, 45071 Orléans Cedex 2, France

[11]ALISTORE-European Research Institute, FR CNRS 3104, 80039 Amiens, France

ABSTRACT: Water electrolysis is considered as a promising way to store and convert excess renewable energies into hydrogen, which is of high value for many chemical transformation processes such as the Haber-Bosch process. However, to allow for the widespread of the polymer electrolyte membrane water electrolysis (PEMWE) technology, the main challenge lies in the design of robust catalysts for oxygen evolution reaction (OER) under acidic conditions since most of transition metal-based oxides undergo structural degradation under these harsh acidic conditions. To broaden the variety of candidate materials as OER catalysts, a cation-exchange synthetic route was recently explored to reach crystalline pronated iridates with unique structural properties and stability. In this work, a new protonated phase $H_{3.6}IrO_4 \cdot 3.7H_2O$, prepared via Sr^{2+}/H^+ cation exchange at room temperature starting from the parent Ruddlesden-Popper Sr_2IrO_4 phase, is described. This is the first discovery of crystalline protonated iridate forming from a perovskite-like phase, adopting a layered structure with apex-linked IrO_6 octahedra. Furthermore, $H_{3.6}IrO_4 \cdot 3.7H_2O$ is found to possess not only an enhanced specific catalytic activity, superior to that of other perovskite-based iridates, but also a mass activity comparable to that of nanosized IrO_x particles, while showing an improved catalytic stability owing to its ability to reversibly exchange protons in acid.

Introduction

Clean production of hydrogen via water electrolysis has long been envisioned as a key process to store and convert renewable energies. Indeed, hydrogen is critical for many applications, such as the transformation of nitrogen into ammonia through the Haber-Bosch process which contributes to more than 1% of the annual energy consumption. Currently, the production of hydrogen still largely relies on fossil fuel reforming, a process which emits CO_2. Water electrolysis ($H_2O = H_2 + ½ O_2$), though considered as an appealing way to achieve clean hydrogen production, only represents around 4% of the annual total, mostly as a side product of the chloralkali process, due to associated technological difficulties.

At present, alkaline water electrolyzers (AWE) are used to realize water electrolysis at industrial scale. However, their performance remains limited owing to the large ohmic drop encountered in the cell that uses alkaline solutions in combination with a diaphragm. Instead, polymer electrolyte membrane water electrolyzers (PEMWE) use a thin protonic conducting membrane, which has the advantage of limiting the ohmic drop in the cell.[1,2] Nevertheless, despite the clear advantages of this technology, the use of acidic conditions as imposed by the protonic conducting membrane leads to drastic instabilities of the catalysts. This is especially true with respect to catalysts for the oxygen evolution reaction (OER), one of the half reactions during water electrolysis that oxidizes water to produce oxygen. Currently, only iridium-based catalysts are considered as sufficiently stable in the harsh acidic conditions required by the PEMWE technology. However, the main issue regarding the use of iridium-based oxides as OER catalysts arises from the scarcity of iridium, whose annual production is even lower

than that of platinum by as much as two orders of magnitude.[3] New chemical strategies to develop better iridium-based OER catalysts both in terms of specific activity (i.e. activity normalized by surface active sites) as well as mass activity are therefore of prime importance for the development of PEMWE.[4,5,6]

Towards this goal of improving the performances of Ir-based OER catalysts, several strategies were recently proposed. Among them, the use of amorphous and hydrated IrO_x as well as iridium-based perovskites as OER catalysts appear promising.[7,8,9,10,11,12,13,14] Nevertheless, despite the high catalytic activity of these OER catalysts, their stability is limited compared to the conventional IrO_2.[15] Specific research efforts are therefore dedicated to limit the dissolution of iridium under OER conditions.[16] Recently, we demonstrated that cationic exchange can be used to prepare a series of novel protonated iridates with improved catalytic stability,[17,18] owing to their ability to reversibly exchange protons under acidic conditions and, therefore, to compensate a charge modification associated with the oxidation of iridium resulting from cation leaching as well as its chemical reactivity with water. This charge compensation via proton exchange helps to avoid the formation of soluble Ir^{3+} or IrO_4^{2-} species which has been considered as the dominating iridium dissolution mechanism.[19] However, the cation exchange strategy was so-far limited to monovalent Li^+/H^+ exchange starting from a parent Li_xIrO_y phase.[20] Cation exchange between divalent cations and protons, such as AEM^{2+}/H^+ exchange (AEM: alkaline earth metal), has not been reported for perovskites so far. Instead, structural degradation of these complex oxides was often observed upon cation leaching under acidic conditions, leading to their poor overall catalytic stability.[21,14,22] This lack of cation exchange is likely due to the great size and charge differences in between AEM^{2+} and H^+, which would introduce significant lattice strain on the 3D-linked IrO_6-network of the perovskite and thus compromise its structural integrity. Therefore, for perovskite-like materials reported up to date such as $SrIrO_3$, Sr_2IrCoO_6 or Ba_2LnIrO_6, no crystalline protonated iridate was obtained via cationic exchange, while the formation of amorphous iridium oxide, usually denoted as $IrO_x{\cdot}nH_2O$, was instead commonly observed on their surfaces.[11,14,22] The structural instability of most of complex oxides, including perovskites, when interacting with H^+ imposes great limits on our ability to design better OER catalysts for PEMWE.

In this work, we report the discovery of a new protonated phase $H_{3.6}IrO_4{\cdot}3.7H_2O$ prepared via Sr^{2+}/H^+ cation exchange at room temperature starting from the parent Ruddlesden-Popper Sr_2IrO_4 phase. This new protonated iridate adopts a layered structure with apex-linked IrO_6 octahedra and is, to the best of our knowledge, the first example of crystalline protonated iridate forming from a perovskite-like phase. Furthermore, we demonstrate that $H_{3.6}IrO_4{\cdot}3.7H_2O$ not only exhibits an enhanced OER activity superior to that for other perovskite-based iridates and even comparable to the performances obtained for nanosized IrO_x particles, but also improved catalytic stability under OER conditions owing to its ability to reversibly exchange protons in acidic conditions.

Experimental section

Synthesis. Sr_2IrO_4 and 6H-$SrIrO_3$ were prepared using a conventional ceramic method as described in previous paper.[23,24] In brief, suitable amount of $SrCO_3$ and Ir black were finely ground and pre-sintered at 900 °C before pressing into a 13 mm diameter pellet. The pellet was then heated in air for 24 h at 1250 °C for Sr_2IrO_4 and 1200°C for 6H-$SrIrO_3$ to obtain a single phase. For the preparation of $H_{3.6}IrO_4{\cdot}3.7H_2O$, Sr_2IrO_4 powder was stirred in 0.1 M $HClO_4$ for 12 h (made from $HClO_4$ 70%, 99,999% trace metals basis, Sigma-Aldrich), then recovered by centrifugation and dried at 55 °C under vacuum for 4 h.

Material Characterization: X-ray diffraction (XRD) data were collected using a BRUKER D8 Advance diffractometer with Cu Kα radiation ($\lambda_{k\alpha1}$ = 1.54056 Å, $\lambda_{k\alpha2}$ = 1.54439 Å). TGA-MS were carried out by heating around 10 to 15 mg of samples under high purity Ar gas from room temperature to 1000 °C at a rate of 5 K min^{-1}.

Solid state ^1H NMR were recorded on a Bruker 4.7 T Avance III spectrometer mounted with a 1.3 mm double-resonance probe head tuned to ^1H at 200 MHz. A 1.3 mm rotor, packed with the sample, was spinning at a 55 kHz MAS rate under nitrogen at room temperature, with no temperature regulation, assuming that the internal rotor temperature is around 50-60°C due to friction effects. The chemical shifts were referenced at 0 ppm with respect to TMS for ^1H and the RF field strength was set to 287 kHz for ^1H. 1024 increments were recorded with a recovery delay of 80 ms. No change was detected when a 1s relaxation delay was used, and we therefore conclude that no signal was lost due to saturation. The longitudinal relaxation T_1 of the main peak was found at 14.3 ms with a saturation-recovery sequence, confirming a paramagnetic environment promoting fast relaxation. All 1D spectra were obtained with a rotor synchronized Hahn echo sequence, with a total echo time of two rotor periods (36.4 μs). The 2D EXSY sequence has been described in previous works and 10 ms exchange delay were used to probe magnetization exchange, either through spin diffusion between close protons species or chemical exchange.[25]

TEM samples were prepared in air by crushing the crystals in a mortar in ethanol and depositing drops of suspension onto holey carbon grids. Electron diffraction (ED) patterns and high angle annular dark field scanning transmission electron microscopy (HAADF-STEM) images were obtained with an aberration-corrected Titan G3 electron microscope operated at 200 kV.

Ex situ X-ray absorption spectroscopy (XAS) measurements at the Ir L_3-edge were carried out at the B18 XAS beamline at the Diamond Light Source. The normalization was done using the Athena software. *Ex situ* XAS measurement at the O K-edge were collected on Beamline 4-ID-C of the Advanced Photon Source (APS) at Argonne National Laboratory. Normalization of the spectra was done using the Athena software.

Brunauer–Emmett–Teller (BET) specific surface areas were measured by N_2 porometry at 77 K using a Micromeritics Triflex instrument. Before measurements, samples were degassed on a Micromeritics Smart VacPrep device for 5 h at 55° C for protonated iridates and 150°C for other oxides. The specific surface area was calculated using BET equations.

For ICP-OES, ~2 mg of active materials were loaded onto a 2*2 cm^2 glassy carbon electrode. The electrode was then held at a current density of 1 mA/cm_{oxide}^2 for 1 h in 20 mL of 0.1 M $HClO_4$ electrolytes. 5 mL of electrolyte was taken for ICP-OES measurements. For the protonated iridate $H_{3.6}IrO_4{\cdot}3.7H_2O$, 2 mg of Sr_2IrO_4 was used and soaked in 20 mL of electrolyte for 10 min to allow for sufficient cation exchange prior to the galvanostatic step. Sr and Ir elements were measured for each sample on a ThermoFisher iCAP 6000

device. Line 346.4, 407.7, 421.5 were used for Sr, and 212.6, 224.2, 236.8 for Ir. The detection error bar of the instrument is ~ 5 to 10%.

Electrochemical Characterization. Electrochemical measurements were carried out at room temperature using a VMP-300 potentiostat (Biologic Co., Claix, France) with a conventional three-electrodes configuration: a glassy carbon electrode with geometric surface area of 0.196 cm^2 as the working electrode, a saturated Ag/AgCl electrode as the reference electrode, and a Pt wire as the counter electrode. The reference electrode was calibrated versus a reversible hydrogen electrode (Gaskatel) prior to the measurements. The CV measurements were performed in 0.1 M $HClO_4$ electrolyte (made from $HClO_4$ 70%, 99,999% trace metals basis, Sigma-Aldrich) at a scan rate of 10 mVs^{-1} (except for Figure 5a and 5b) with a rotating speed of 1600 rpm. Potentials are corrected with iR drop and reported versus RHE (resistance ≈ 28 to 32 Ω for 0.1 M $HClO_4$). The catalysts were drop-casted onto the working electrode. The drop-casting ink was prepared by dispersing 10 mg catalyst powders and 2 mg ethylene black carbon (Alfa Aesar 99.9%) in 1.940 mL of tetrahydrofuran (THF; Sigma-Aldrich 99.9%) and 0.060 mL of Nafion binder (5% weight, Ion Power). The loading of active material was 50 µg (10 µL ink) per electrode.

Ex situ XRD measurements on the electrode. Ex situ XRD data as shown in Figure 5d were collected at different potentials on self-standing PTFE electrodes. The PTFE electrodes were prepared by mixing $H_{3.6}IrO_4{\cdot}3.7H_2O$ together with 10 wt% ethylene black carbon and 5 wt% PTFE in ethanol, and then laminating the paste several times to obtain films of ~ 25 µm thickness. The three electrodes used were glassy carbon rods with a piece of the PTFE film as the working electrode, calomel electrode (0.240 V vs. SHE) as the reference electrode and YP50 Carbon as the counter electrode. The working and counter electrodes were separated using 3 Whatman glass fiber separators fully soaked in the 0.1 M $HClO_4$ electrolyte.

Exfoliation: $H_{3.6}IrO_4{\cdot}3.7H_2O$ powders were stirred in a TBAOH solution for 7 days until a suspension with an indigo-blue color was obtained. The suspension was then sonicated for 1 h for further exfoliation. As TBA^+ ions form insoluble salts in $HClO_4$ electrolytes, the suspension was centrifuged at 6000 rpm for 1 h and washed twice with H_2O to remove the excess TBA^+ ions. The concentration of iridium in the final suspension was detected by ICP-OES and this suspension was directly drop-casted on glassy carbon electrodes for electrochemical measurements.

Results and discussion

Synthesis, composition and structure of the newly formed protonated phase. The novel protonated iridate H_xIrO_y was obtained via a cation exchange of H^+/Sr^{2+} starting from the Sr_2IrO_4 Ruddlesden-Popper (RP) phase, as illustrated in Figure 1. In brief, Sr_2IrO_4 powder was stirred in 0.1 M $HClO_4$ for 12 h, then recovered by centrifugation and dried at 55 °C under vacuum. The formation of a novel phase was confirmed by powder X-ray diffraction (XRD, Figure 1b) collected on the sample recovered after drying, where peaks that cannot be indexed with the unit cell of the parent Sr_2IrO_4 phase were observed. Complete removal of Sr^{2+} from Sr_2IrO_4 was confirmed by energy-dispersive X-ray (EDX) analysis (see Supplementary Information (SI), Figure S1). The composition of the newly obtained H_xIrO_y phase was then characterized by thermogravimetric analysis coupled with mass spectrometry (TGA-MS) (Figure 2a, detailed in the Experimental Section). According to the TGA-MS results, H_xIrO_y first loses structural water to form rutile-type IrO_x in the temperature range of 140 - 400 °C, before decomposing into metallic Ir when heating up to 1000°C under Ar. The formation of rutile-IrO_x at 400 °C and Ir at 1000 °C was confirmed by powder X-ray diffraction data collected after treatment at the corresponding temperatures, as shown in Figure S2. From the weight loss measured by TGA, the total H_2O content in the iridate is estimated to be 5.50(5) per Ir (mol/mol). Coupling this result to the amount of oxygen loss during the decomposition into Ir, the composition of the newly obtained hydrated iridate is thus determined to be $H_{3.6}IrO_4{\cdot}3.7H_2O$, given that Sr^{2+} is fully removed and replaced by H^+ during the cation exchange, as suggested by EDX analysis (Figure S1). Furthermore, despite the striking size and charge differences existing between H^+ and Sr^{2+}, the as-prepared particles largely retained their shape and size during the cation exchange, as observed by SEM (inset of Figure 1a and 1b). Nevertheless, cracks can be observed on the particles after the cation exchanged step, possibly forming from the exfoliation process occurring during the insertion of H^+/H_2O into the layered iridate and the subsequent drying step.

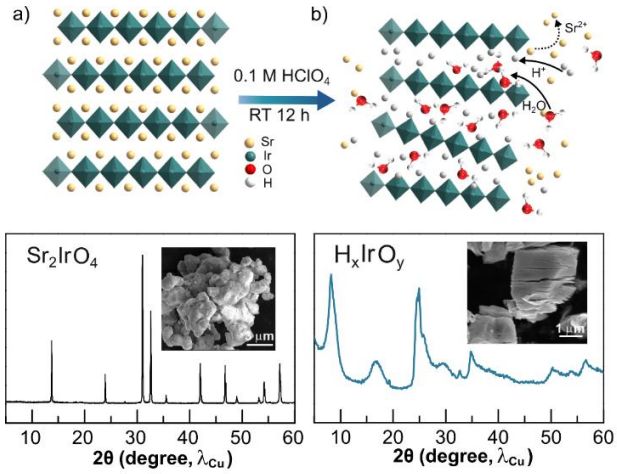

Figure 1. a Crystallographic structure of the parent Sr_2IrO_4 phase and **b** schematic representation of the hydrated $H_{3.6}IrO_4{\cdot}3.7H_2O$ phase obtained after cation exchange as well as their corresponding powder XRD patterns (bottom) and SEM images (insets).

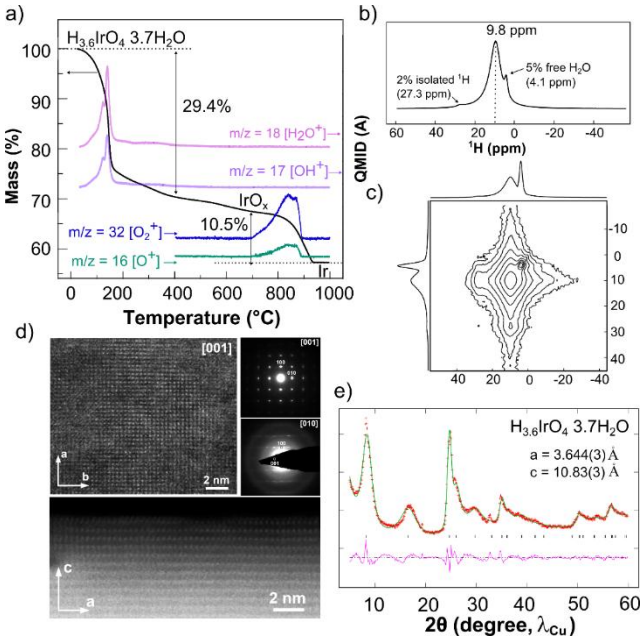

Figure 2. a Thermogravimetric analysis with mass spectrometry (TGA-MS) curve, **b** ^1H Magic Angle Spinning solid-state nuclear magnetic resonance (NMR) spectra, **c** ^1H 2D EXSY-NMR spectra with 10 ms exchange delay, **d** HAADF-STEM images and ED patterns along the [001] and [010] directions and **e** Le Bail fit of the powder XRD pattern collected for the $H_{3.6}IrO_4{\cdot}3.7H_2O$ hydrated phase.

To investigate the proton environment in $H_{3.6}IrO_4{\cdot}3.7H_2O$, solid-state ^1H ultra-fast magic angle spinning nuclear magnetic resonance (MAS-NMR) measurements were carried out (Figure 2b and 2c). Ultra-fast MAS at 55 kHz is expected to minimize the dipolar couplings and only two extremely weak spinning sidebands resulting from anisotropic paramagnetic and dipolar interactions were detected on both sides of the main peak. As shown in Figure 2b, one major broad ^1H peak centered at 9.8 ppm is observed and can be assigned to structural protons (in comparison to water protons) in $H_{3.6}IrO_4{\cdot}3.7H_2O$. Given that no other large component was detected apart from this intense peak, it is reasonable to conclude that, in $H_{3.6}IrO_4{\cdot}3.7H_2O$, the protons bounded to IrO_6 octahedra are in fast exchange with structural water molecules so that anisotropic interactions are reduced by fast motion of the hydrogen atoms which gives rise to a broad ^1H signal. Apart from this main peak, a sharp shoulder peak is observed at 4.1 ppm and can be assigned to free or weakly hydrogen bounded H_2O,[26,27] suggesting the presence of a small portion of "free" water (5%), i.e. water molecules not interacting with structural protons, for the newly formed iridate. The amount of remaining free water is small, as ultra-fast MAS is performed under a dry atmosphere, and friction-induced heating leads to an internal temperature of 50-60°C, which is usually sufficient to remove weakly bounded water molecules. The magnetization exchange between the main peak and the free water is not detected, consistently suggesting that protons from the free water are surface-adsorbed water molecules far away from the bulk protons. Furthermore, a very small fraction of isolated protons (2%) was also observed at 27.3 ppm. Comparing the 2D exchange spectra obtained using either a 10 ms exchange delay (Figure 2c) or an 18 µs (1 rotor period) exchange delay, one clearly sees the cross-peak demonstrating some magnetization transfer between the peak at 27.3 ppm and the main 9.8 ppm peak, suggesting either slow exchange and/or close proximity promoting spin diffusion. It is likely that these protons at 27.3 ppm may belong to Ir-OH groups instead of Ir-OH_2 entities as only 3.6 hydrogens are bound to the iridium apical oxygens instead of 4 (according to the TGA-MS analysis discussed above).

As observed in the XRD pattern in Figure 1b, the newly obtained $H_{3.6}IrO_4{\cdot}3.7H_2O$ is poorly crystallized, challenging its structural characterization solely by powder XRD. Nevertheless, a Le Bail refinement against the X-ray diffraction data of $H_{3.6}IrO_4{\cdot}3.7H_2O$ using a primitive tetragonal cell with $a \approx 3.644(3)$ Å, $c \approx 10.83(3)$ Å was conducted (Figure 2e), and a proposed structure is shown in Figure 3. Electron diffraction (ED) data and high angle annular dark field scanning transmission electron microscopy (HAADF-STEM) images were then taken (Figure 2d), with nevertheless the limitation that structural water is lost under vacuum in the TEM column. As a result, the ED data of $H_{3.6}IrO_4{\cdot}3.7H_2O$ could be indexed into a primitive tetragonal unit cell with $a \approx 3.6$ Å, $c \approx 5.7$ Å, or a body-centered cell with $\sqrt{2} \times \sqrt{2} \times 2$ expansion ($a \approx 5.1$ Å, $c \approx 11.4$ Å), where the decreased c parameter when compared to the XRD Le Bail fitting is consistent with the loss of structural water. Furthermore, the HAADF-STEM image in the [001] direction reveals that the $H_{3.6}IrO_4{\cdot}3.7H_2O$ phase consists of square layers of iridium with an Ir-Ir distance of 3.6 Å, characteristic of apex-linked IrO_6 octahedra (~ 3.8[23] and ~ 3.0[20] Å in general for corner- and edge-shared IrO_6, respectively), while the image in the [010] direction shows that the apical oxygen of the IrO_6 octahedra are facing each other. One can thus observe that the H^+/Sr^{2+} cation exchange led to a structural modification of the parent Sr_2IrO_4 RP phase (Figure 1a). Indeed, while the apex-linked IrO_6 octahedra in each iridium layer in the *ab* plane is retained, the cation exchange triggers gliding of the iridium layers along the [110] direction alternatively so that every IrO_6 octahedra sits on top of each other. This gliding is possibly driven by protonation of apical oxygen that screens the repulsion between each oxygen layers combined with the intercalation of a large amount of structural water molecules into interstitial sites in the new structure, as depicted in Figure 3. Moreover, as suggested by the ^1H NMR results (Figure 2b), the apical oxygens are presumably protonated with almost two protons so that all the protons sit in a similar environment and are in direct exchange with structural water molecules that sit in the interstitials. Some oxygens might be protonated with one only proton (proton vacancies are not shown in Figure 3), corresponding to the weak proton signal at 27.3 ppm, as discussed above.

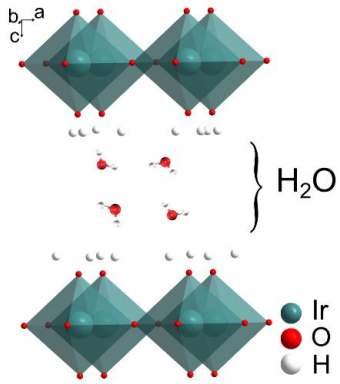

Figure 3. Schematic representation of the structure of the new hydrated $H_{3.6}IrO_4 \cdot 3.7H_2O$ phase, where apical oxygens are represented as fully protonated. The corner-shared octahedral as well as the protons positions are extrapolated for the structural model deduced from the XRD, TEM and NMR results, while the structural water molecules which are interacting with protons on apical oxygen are schematically represented in between the iridium layers.

Altogether, these results indicate that $H_{3.6}IrO_4 \cdot 3.7H_2O$ is, to the best of our knowledge, the first pronated iridate with a perovskite-like structure reported to date. Other iridium-based perovskites such as $SrIrO_3$ or Sr_2IrFeO_6 have been observed to either collapse or to heavily dissolve before precipitating into amorphous hydrated IrO_x when placed in acidic conditions.[11,14,22] The successful H^+/Sr^{2+} exchange to form $H_{3.6}IrO_4 \cdot 3.7H_2O$ starting from the parent phase Sr_2IrO_4 certainly benefits from the structural flexibility offered by the layered nature of the parent RP phase in which cations can tunnel in/out without deconstructing the in plane corner-shared coordination of the IrO_6 octahedra. Furthermore, RP phases are known to accommodate interstitial anions such as O^{2-} within their structure[28,29], thus allowing the co-intercalation of structural water molecules during the cation exchange which, by hydrogen bonding, stabilizes the structural protons. Unlike the 2D RP phase, the H^+/Sr^{2+} exchange in cubic or hexagonal perovskite such as $SrIrO_3$ would introduce significant lattice strain on the 3D IrO_6-network and thus compromise the structural integrity of the parent phase, leading to a dissolution of the phase and a precipitation of amorphous IrO_x compounds on its surface.[18] Moreover, $H_{3.6}IrO_4 \cdot 3.7H_2O$ also differs distinctively from the recently reported protonated iridates, such as the H_xIrO_3 and H_xIrO_4 family that were previously synthesized via a Li^+/H^+ exchange step in acid from the parent β-Li_2IrO_3 and Li_3IrO_4 phases, respectively.[17,20] Unlike the H_xIrO_3 and H_xIrO_4 series whose structures consist of the edge-sharing IrO_6 octahedra conserved from their parent phases during cation exchange, the newly obtained $H_{3.6}IrO_4 \cdot 3.7H_2O$ contains layers of corner-sharing IrO_6 octahedra with a large amount of structural water. This layered perovskite-like structure adopted by $H_{3.6}IrO_4 \cdot 3.7H_2O$ is also uniquely distinct from previously reported IrOOH,[30] which consists of trigonal layers of edge-sharing octahedra.

Electrocatalytic properties towards OER. Having determined the crystal structure for the newly obtained $H_{3.6}IrO_4 \cdot 3.7H_2O$ phase, its electrochemical performance towards water oxidation was then tested in 0.1 M $HClO_4$ and compared with that of the pristine Sr_2IrO_4 (Figure 4a and Figure S3). As a result, no major difference in their respective redox activity was observed between these two phases (inset of Figure 4a). This observation indicates that the parent Sr_2IrO_4 phase quickly transforms into the protonated phase after exposure to the acidic environment, reinforcing that the cation Sr^{2+}/H^+ exchange is fast in acidic conditions. Nevertheless, while their redox behaviors were found similar, such a phase transformation induces a significant change in the specific surface area of the iridate, as revealed by estimating the specific surface by Brunauer-Emmett-Teller (BET) method. Indeed, the BET surface area of the pristine Sr_2IrO_4 was measured to be 0.30 m^2/g, a limited specific surface area commonly observed for crystalline oxide catalysts synthesized by solid-state reaction at high temperature, while the BET surface area of the exchanged phase $H_{3.6}IrO_4 \cdot 3.7H_2O$ was measured to be 4.01 m^2/g, ~13 times larger than that of the pristine Sr_2IrO_4 before exchange. This drastic gain in surface area presumably results from the cracks observed by SEM, as shown in Figure 1b. Therefore, caution must be exercised when normalizing the OER performances of a catalyst using the BET surface area of the pristine compound, especially when the catalyst undergoes phase transformation upon interaction with the electrolyte (e.g. ion exchange, dissolution, element leaching). For instance, if the OER performances for Sr_2IrO_4 were normalized by the BET surface area of the pristine phase (~ 0.3 m^2/g), a current as high as 10 mA/cm^2_{oxide} would be obtained at 250 mV overpotential (red dashed line in Figure 4b), outperforming most of iridium-based oxides reported to date. However, the "real" performances for the $H_{3.6}IrO_4 \cdot 3.7H_2O$ phase are found one order of magnitude lower, but still among the most active iridate oxides previously reported (red line in Figure 4b).

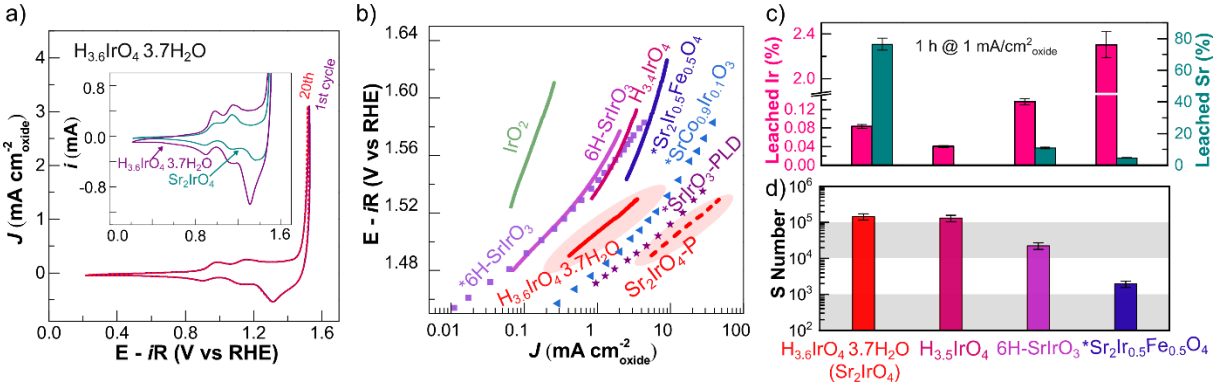

Figure 4. a Representative CV scans obtained directly from the cation-exchanged phase $H_{3.6}IrO_4 \cdot 3.7H_2O$ compared to those obtained from the parent phase Sr_2IrO_4 with no exchange prior to OER measurements. **b** Tafel slopes for the OER activity normalized by BET surface area for selected iridium-based catalysts compared to the one obtained for $H_{3.6}IrO_4 \cdot 3.7H_2O$ when normalized with the BET surface measured before (red dash line) or after (red solid line) cation exchange. * refers to data extracted from previous reports (6H-$SrIrO_3$,[21] $Sr_2Ir_{0.5}Fe_{0.5}O_4$,[14] $SrCo_{0.9}Ir_{0.1}O_3$[21] and $SrIrO_3$-PLD[11]). **c** Amount of iridium and strontium detected by ICP measurements after electrochemical testing for 1 h at 1 mA/cm^2_{oxide} (top, error bar: 10 %) as well as, **d** Calculated stability number (S-number) for $H_{3.6}IrO_4 \cdot 3.7H_2O$ compared to selected iridium-based catalysts (bottom, error bar 20 %). * refers to data extracted from previous report (*$Sr_2Ir_{0.5}Fe_{0.5}O_4$[14]).

As shown in Figure 4b, a current density of 4.0 mA/cm^2_{oxide} is obtained for $H_{3.6}IrO_4 \cdot 3.7H_2O$ at an overpotential of 300 mV, ~ 2 fold to that of Ir^V-based $Sr_2Ir_{0.5}Fe_{0.5}O_4$ (2.0 mA/cm^2_{oxide}, BET = 0.75 m^2/g), ~5 fold to that of $H_{3.5}IrO_4$ (0.75 mA/cm^2_{oxide}, BET = 2.2 m^2/g) and ~7 fold that of 6H-$SrIrO_3$ (0.56 mA/cm^2_{oxide}, BET = 1.0 m^2/g). Only the OER performance obtained for $SrIr_{0.1}Co_{0.9}O_3$ (~9 mA/cm^2_{oxide}, BET = 0.175 m^2/g) and for epitaxial $SrIrO_3$ film (~20 mA/cm^2) were found to be greater, with nevertheless doubts arising from the proper normalization of such catalysts undergoing phase transformation and surface reconstruction into IrO_x in acid, as pointed out in a recent work.[31] Interestingly, the newly obtained $H_{3.6}IrO_4 \cdot 3.7H_2O$ phase exhibits greater OER performances when compared to another layered iridate, namely $H_{3.5}IrO_4$.[20] The superior activity of $H_{3.6}IrO_4 \cdot 3.7H_2O$ can be tentatively explained by the corner-sharing IrO_6 octahedral network within its structure, with earlier reports proposing that catalysts containing corner-shared IrO_6 octahedra are preferred for the OER.[32] Furthermore, the presence of large amount of structural water in $H_{3.6}IrO_4 \cdot 3.7H_2O$ might influence the formation energy of the OER intermediates (*OH, *O, and *OOH), as proposed in earlier reports where hydroxylated RP-perovskite $Sr_3FeCoO_{7-\delta}$ was found to have enhanced OER activity.[33]

Having established that the OER performances measured for $H_{3.6}IrO_4 \cdot 3.7H_2O$ are among the best for iridium-based oxide catalysts, we then investigated the stability of this catalyst in OER conditions. The amount of dissolved iridium after galvanostatic holding at 1.0 mA/cm^2_{oxide} for 1 h was tracked down by inductively coupled plasma atomic emission spectroscopy (ICP-OES) measurements (see details in the Experimental Section). As shown in Figure 4c, the percentage of leached iridium for several iridium-based oxides trends as follows: $H_{3.5}IrO_4$ < $H_{3.6}IrO_4 \cdot 3.7H_2O$ < 6H-$SrIrO_3$ << $Sr_2Ir_{0.5}Fe_{0.5}O_4$, suggesting that $H_{3.5}IrO_4$ and $H_{3.6}IrO_4 \cdot 3.7H_2O$ are relatively more stable (see Table S1 for the raw current and measured potentials for each catalyst). Moreover, the relative stability of this protonated phase is reinforced by the evaluation of the 'stability number' (S-number), previously introduced as given by the ratio of gaseous oxygen generated during OER and the amount of dissolved iridium[22]. For $H_{3.6}IrO_4 \cdot 3.7H_2O$, the S-number is calculated to be ~10^5, approximating the same as obtained for $H_{3.5}IrO_4$ (~10^5) and greater than that for 6H-$SrIrO_3$ (~10^4) and $Sr_2Ir_{0.5}Fe_{0.5}O_4$ (~10^3). As a comparison, rutile-IrO_2 and amorphous IrO_x have been reported with an S-number of ~10^6 and ~10^5, respectively.[22] Thus, the S-numbers for protonated iridates $H_{3.6}IrO_4 \cdot 3.7H_2O$ and $H_{3.5}IrO_4$ are similar to IrO_x and only below rutile-IrO_2, while the OER activity of $H_{3.6}IrO_4 \cdot 3.7H_2O$ outperforms both IrO_x and IrO_2. This can be due to the formation of under-coordinated sites on the surface of protonated iridate phases, while IrO_2 remains fully coordinated, as previously suggested.[34,35] Furthermore, it is interesting to point out that $H_{3.6}IrO_4 \cdot 3.7H_2O$ prepared from the parent RP-Sr_2IrO_4 phase is significantly more stable than the Fe-doped RP-perovskite $Sr_2Ir_{0.5}Fe_{0.5}O_4$, as seen by the increase of ~2 orders of magnitude in S-number (Figure 4c). This difference can be easily explained by the fact that $Sr_2Ir_{0.5}Fe_{0.5}O_4$ tends to heavily dissolve in acid while Sr_2IrO_4 undergoes cation exchange to form the protonated iridate, $H_{3.6}IrO_4 \cdot 3.7H_2O$. These differences highlight that the substitution of Ir by a soluble element in acid (Fe) will only destabilize the layered iridate because the leaching of Fe will break the bonding around IrO_6, causing heavy dissolution of undercoordinated Ir in $Sr_2Ir_{0.5}Fe_{0.5}O_4$.

Proton exchange properties. To further understand the electrochemical behavior of $H_{3.6}IrO_4 \cdot 3.7H_2O$ and its ability to reversibly exchange protons in acidic conditions, its redox behavior was investigated in the potential range of 0.3 to 1.4 V vs RHE, prior to the OER potential. As shown in Figures 5a and 5b, two redox peaks are visible for $H_{3.6}IrO_4 \cdot 3.7H_2O$ in this potential range, with a first one observed at ~0.92 V vs RHE with a peak separation of ~50 mV and a second one at ~1.14 V vs RHE associated with a small peak separation of ~5 mV. These redox features are distinctively different to that reported for IrO_2,[22] IrO_x,[22,36] 6H-$SrIrO_3$[21] or $SrIrO_3$ epitaxial thin films[22], for instance. To gain further insight into the kinetics of these two redox peaks, cyclic voltammograms were collected as a function of the scan rate (Figure 5a and 5b). As a result, the intensity of the first redox peak at ~0.92 V vs RHE was found to be proportional to the square root of the scan rate, suggesting a bulk diffusion-limited redox process (Figure 5b). The intensity of the second redox peak at ~1.14 V vs RHE was found proportional to the scan rate (Figure 5a), suggesting a non-diffusion-limited surface proton exchange, agreeing with the observed small peak separation (~5 mV).

These results are consistent with the *ex situ* XRD data collected at different potentials for $H_{3.6}IrO_4 \cdot 3.7H_2O$ (see Experimental Section). It is worth mentioning that the *ex situ* XRD data collected from an electrode are slightly different from a powder sample, possibly due to the preferred orientation of the layered $H_{3.6}IrO_4 \cdot 3.7H_2O$ and a slight loss of the structural water during the electrode preparation. Nevertheless, from these measurements one can observe that, as shown in Figure 5d, when scanning from the OCV to 1.3 V vs RHE, the (001) diffraction peak of $H_{3.6}IrO_4 \cdot 3.7H_2O$ at ~ 9° (λ_{Cu}) is shifted to higher angle, indicating a decrease in the *c* lattice parameter. This bulk contraction in the *c* direction (~ 0.8 Å), which is much greater than what can be expected solely from the shortening of Ir-O bonds due to the oxidation of Ir^{4+} to Ir^{5+}, can be ascribed to the removal of structural water and protons from $H_{3.6}IrO_4 \cdot 3.7H_2O$, a bulk process which is therefore kinetically diffusion-limited in agreement with the electrochemical results. From 1.3 V to ~1.5 V vs RHE where the OER occurs, no obvious change was observed in the XRD data, consistent with a surface process. When scanning back to the starting potential, a small shift of the (001) diffraction peak at ~10° as well as a change of the (003) and (110) diffraction peaks was observed, presumably due to the re-protonation of $H_{3.6}IrO_4 \cdot 3.7H_2O$ in this potential range. Nevertheless, the XRD data collected back at the OCV for $H_{3.6}IrO_4 \cdot 3.7H_2O$ does not superimpose with that of the pristine phase, suggesting an irreversible loss of structural water upon cycling. Several reasons could explain this loss. First, reinsertion of structural water can be hindered by the presence of hydrophobic PTFE binder used for preparing the electrode. Second, the diffusion-limited structural exchange of water might be kinetically hindered.

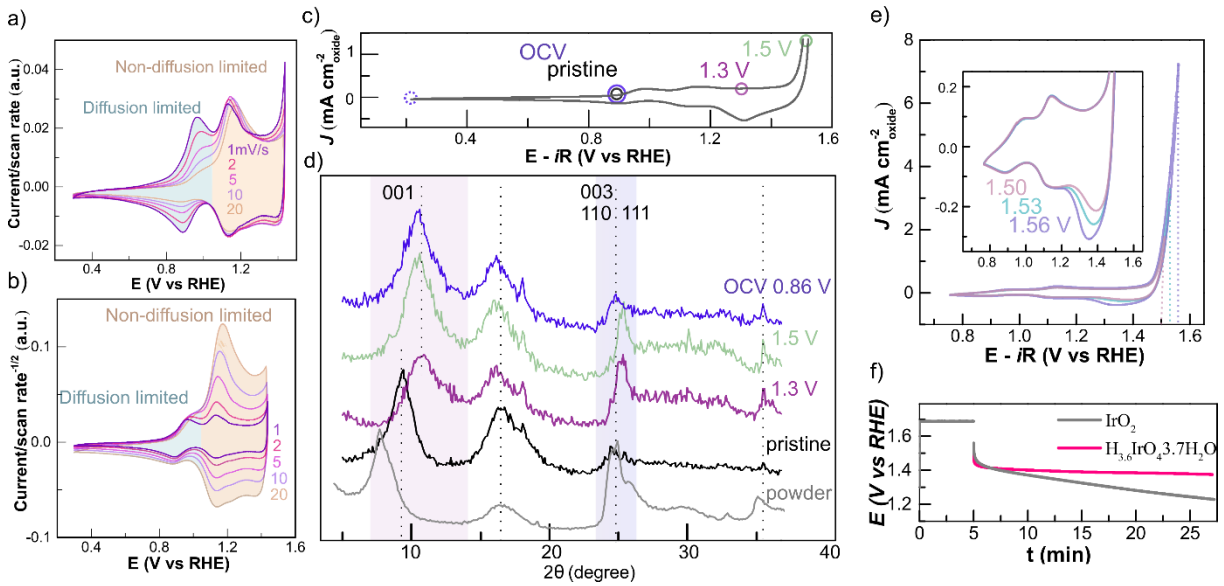

Figure 5. CV scans recorded at different scan rate for $H_{3.6}IrO_4 \cdot 3.7H_2O$ normalized by **a** the scan rate or **b** the square root of the scan rate. **c** typical CV scan recorded for an electrode from which **d** *ex situ* XRD patterns were collected at different potentials. **e** CV scans recorded for the same electrode but with different voltage cutoff (1.50, 1.53 and 1.56 V vs. RHE) and **f** evolution of the potential measured for $H_{3.6}IrO_4 \cdot 3.7H_2O$ compared to IrO_2 after potentiostatic holding at 1.65 V vs. RHE for 5 minutes.

Finally, in addition to these two redox features, a reduction peak at ~1.4 V vs. RHE is observed. Further investigation reveals that the intensity of this reduction peak is proportional to the cut-off potential during the OER (1.50, 1.53 V or 1.56 V vs. RHE, as shown in Figure 5e). This result implies that the intensity of the reduction peak is related to the amount of charge passed at potentials above 1.4 V vs. RHE. Therefore, this behavior suggests that the oxidation state of the iridate is modified during the OER. In order to confirm this hypothesis, tests were made during which $H_{3.6}IrO_4 \cdot 3.7H_2O$ was held at 1.65 vs RHE for 5 min before opening the circuit and monitoring the potential decay upon time. As shown in Figure 5f, the potential of the hydrated iridate rapidly stabilizes at around 1.4 V vs RHE, unlike crystalline IrO_2 for which the potential constantly decays for more than 20 minutes down below 1.2 V vs. RHE. This measurement further confirms that the active form of the iridate is an oxidized phase formed at the OER potential and that this oxidation state is maintained even in contact with a strongly acidic solution. In contrast, when holding IrO_2 at OER potential, no bulk oxidation is occurring and the potential slowly decays back to its initial open circuit potential. Altogether, these measurements show that $H_{3.6}IrO_4 \cdot 3.7H_2O$ undergoes three different redox processes in acidic conditions: the first one being a bulk diffusion-limited process at ~0.92 V vs RHE involving de-/intercalation of H_3O^+ within the structure of the layered iridate, a second non-diffusion-limited process at ~1.14 V vs RHE which can be attributed to the surface deprotonation/protonation and a third oxidation process occurring at the OER potential.

Electronic signature of oxygen species in the hydrated iridate. Having established the unique ability for $H_{3.6}IrO_4 \cdot 3.7H_2O$ to reversibly exchange protons and structural water before and during the OER, our attention then turned to understanding the electronic properties of this phase. XAS measurements at the O K-edge were thus carried out. As shown in Figure 6a (and Figure S4), the first set of peaks at ~ 527.8-528.5 eV for Sr_2IrO_4, which are normally ascribed to the transition to unoccupied O 2p hybridized with Ir 5d corresponding to t_{2g} frontier orbitals,[37] respectively, gained significant intensity with a shifting to lower energy after the H^+/Sr^{2+} cation exchange and the formation of $H_{3.6}IrO_4 \cdot 3.7H_2O$. A similar change of this pre-edge feature was previously observed for amorphous IrO_x at elevated potential during the OER,[38] and was explained by the formation of electrophilic "O^-" oxygen species following the deprotonation of the surface of the catalyst. This explanation would be consistent with the slight oxidation of Ir^{4+} in Sr_2IrO_4 into $Ir^{4.4+}$ in $H_{3.6}IrO_4.3.7H_2O$, as observed by XAS measurements at the Ir L-edge (Figure S5), as well as consistent with the O K-edge data collected for the partially delithiated α-$LiIr^{5+}O_3$ which is known to undergo lattice oxygen oxidation upon oxidation (delithiation) (grey line in Figure 6a). In order to assess this explanation, we intentionally removed structural water molecules from $H_{3.6}IrO_4 \cdot 3.7H_2O$ via an exfoliation process achieved by vigorously shaking $H_{3.6}IrO_4 \cdot 3.7H_2O$ in water, which 'frees' structural water in between the exfoliated iridate layer (Figure 6b, Figure S6). This dehydration step was confirmed by the TGA-MS results which gives a composition of H_4IrO_4 for the dehydrated phase (Figure 6c). Furthermore, ^1H NMR shows that protons bounded to IrO_6 octahedra in H_4IrO_4 have a different average chemical shift of 11.9 ppm when compared to $H_{3.6}IrO_4 \cdot 3.7H_2O$ (9.8 ppm, Figure 2) as a result of the lack of interactions with neighboring water molecules (Figure 6d). Combining these results with the XAS ones, we find that the intensity and the energy of the aforementioned pre-feature at the oxygen K-edge are dependent on the presence of the structural water in iridates (Figure 6a). Indeed, a drastic loss of intensity is observed for the pre-edge feature of the dehydrated H_4IrO_4 which energy is also found to shift towards greater energy (see Figure S4 for a zoom in), alike the one observed for Sr_2IrO_4. These results suggest that the presence of structural water might be responsible for the presence of the low energy pre-edge feature previously ascribed to the formation of electrophilic "O^-" species. Therefore, caution must be exercised when attempting to identify surface species

during the OER using XAS data, especially for amorphous hydrated compounds such as IrO_x.

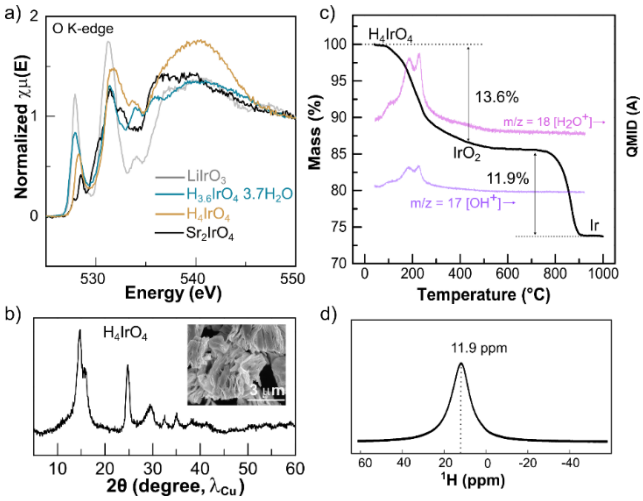

Figure 6. a *Ex situ* XAS measurements at the O K-edge recorded for $H_{3.6}IrO_4{\cdot}3.7H_2O$ compared to $LiIrO_3$, Sr_2IrO_4 as well as compared to the dehydrated H_4IrO_4 phase. **b** Powder XRD pattern, **c** TGA-MS data and **d** ^1H NMR spectra collected for the dehydrated H_4IrO_4 phase.

Toward the enhancement of the mass activity by exfoliation. While the specific activity of the newly obtained hydrated iridate $H_{3.6}IrO_4{\cdot}3.7H_2O$ was found among the best for Ir-based catalysts in acidic conditions (Figure 4b), the OER activity normalized by the mass of iridium is also of prime importance for the deployment of PEMWE at large scale, owing to the extreme scarcity of iridium.[4] In order to increase the mass normalized OER activity of $H_{3.6}IrO_4{\cdot}3.7H_2O$, we took advantage of its 2D structure to partially exfoliate the particles and thereby further increase the specific surface area. To do so, we employed a route previously described for the exfoliation of layered oxides such as K_xIrO_y and $NaRuO_2$.[39,40] After Sr^{2+}/H^+ cationic exchange, the hydrated $H_{3.6}IrO_4{\cdot}3.7H_2O$ phase was stirred in a TBAOH solution for 7 days to insert TBA^+ inside the structure, following by sonication for 1 h to induce exfoliation (Figure 7a, see details in the Experimental section). The suspension containing the exfoliated iridate layers was directly drop-casted onto the glassy carbon electrodes for electrochemical measurements, while the concentration of iridium in the suspension was estimated by ICP-OES. By SEM imaging, we could confirm the relative success of the exfoliation where the micron-sized particles are found to break down into smaller ones (inserts in Figure 7a). Nevertheless, no homogeneous dispersion of single sheets was obtained using this method, unlike previously reported for other layered compounds.[40] An enhancement of the OER current by a factor close to 2 at η = 300 mV can be seen (Figure 7b), comparing the mass normalized OER activity of these partially exfoliated particles with the one obtained for micron-size $H_{3.6}IrO_4{\cdot}3.7H_2O$. This enhancement renders the mass normalized activity measured for this new hydrated phase second only to nano core-shell $IrNiO_x$ catalysts,[41] and being competitive with that reported for IrO_x particles as small as 2nm. Therefore, with further optimization of the exfoliation procedure by either heating to improve the TBA^+ exchange into the hydrated $H_{3.6}IrO_4{\cdot}3.7H_2O$ phase or by using a harsher sonication protocol, one can expect that this newly obtained phase could even overpass the mass activity for the best Ir-based nanocatalysts reported to date.

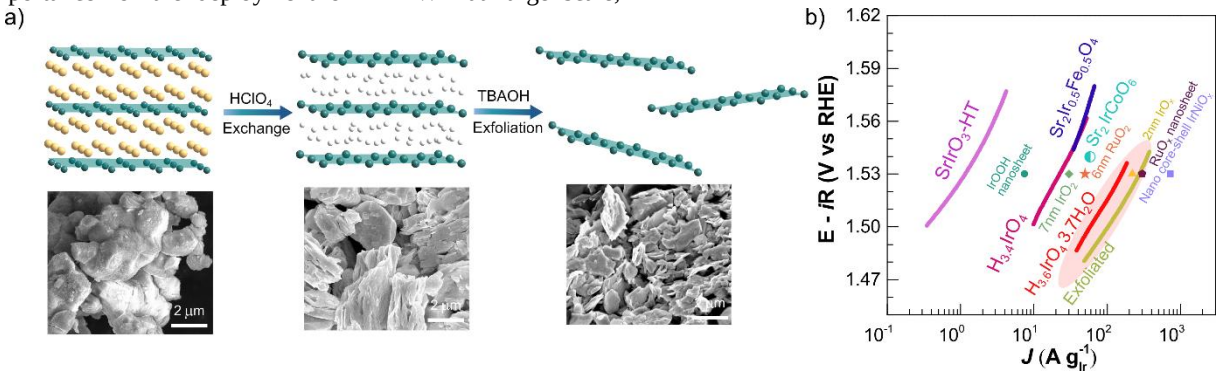

Figure 7. a Schematic representation of the cationic Sr^{2+}/H^+ exchange starting from Sr_2IrO_4 to form the hydrated $H_{3.6}IrO_4{\cdot}3.7H_2O$ phase followed by the exfoliation strategy to decrease the particle size of the newly obtained hydrated phase. **b** Tafel slope for the mass normalized OER activity of $H_{3.6}IrO_4{\cdot}3.7H_2O$ compared to results previously reported for selected iridium- and ruthenium-based catalysts (IrOOH nanosheet,[42] 7 nm IrO_2,[43] 6 nm RuO_2,[43] Sr_2IrCoO_6,[14] 2 nm IrO_x,[44] RuO_x nanosheet,[40] Nano core-shell $IrNiO_x$[41]).

Conclusion

In conclusion, we have demonstrated the first successful Sr^{2+}/H^+ cationic exchange in the 2D Ruddlesden-Popper Sr_2IrO_4 to prepare a new protonated and hydrated compound, $H_{3.6}IrO_4{\cdot}3.7H_2O$. While this hydrated phase retains the corner-shared IrO_6 octahedral layers from the parent Ruddlesden-Popper phase, gliding of the IrO_6 octahedra sheets was observed, resulting in their alignment along the *c*-axis. Though this unique structural configuration is extremely unfavored for an RP phase, the protonation of the apical oxygen screens the charge from the oxygen anions and hence stabilizes the structure. In addition, the intercalation of interstitial water molecules further stabilizes the structure through hydrogen bonds forming between the protonated apical oxygen and the water molecules. Moreover, the newly obtained hydrated iridate phase shows very promising performances as OER catalysts in acidic conditions, with a BET-normalized activity outperforming IrO_2 and some perovskites (e.g. 6H-$SrIrO_3$) while approaching to those reported for $SrIrO_3$ epitaxial films. More importantly, our stability study shows that while 6H-$SrIrO_3$ is

unstable in acidic conditions under anodic polarization, the newly obtained $H_{3.6}IrO_4 \cdot 3.7H_2O$ phase shows relatively limited iridium leaching as well as stable performances under these drastic conditions. Coupling the electrochemical study with the *ex situ* XRD data, we could postulate that this improved stability is in part due to the reversible exchange of protons as well as structural water occurring prior and during the OER. Indeed, these exchanges, especially the proton exchange, allows for the phase to counterbalance the charge associated with the OER and therefore help to avoid the formation of soluble Ir^{3+} or IrO_4^{2-} species which has been considered as the dominating iridium dissolution mechanism.[17,19] Finally, we demonstrate the flexibility of this new 2D phase which can be partially exfoliated to decrease the particle size and reach mass normalized OER performances competing with the ones previously reported for 2 nm IrO_x particles. We therefore believe that such hydrated 2D structure represents a unique opportunity to 1) limit the drastic iridium leaching often encountered for complex iridium-based catalysts and 2) achieve greater mass normalized OER performances that is a prerequisite for scaling up clean production of hydrogen by using PEMWE.

ASSOCIATED CONTENT

Supporting Information. SEM-EDX analysis, XRD data of $H_{3.6}IrO_4 \cdot 3.7H_2O$ at different temperatures, Electrochemical conditions for the galvanostatic test, XAS measurements at the Ir L_3-edge and O K-edge, as well as ED data of H_4IrO_4. This material is available free of charge via the Internet at http://pubs.acs.org.

AUTHOR INFORMATION

Corresponding Author

* alexis.grimaud@college-de-france.fr

Author Contributions

The manuscript was written through contributions of all authors.

Funding Sources

A.G. and R.Z. acknowledge financial support from the ANR MIDWAY (Project ID ANR-17-CE05-0008). J.C. and H.L. were supported by the National Science Foundation under grant no. DMR-1809372. Use of the Advanced Photon Source at Argonne National Laboratory was supported by the US Department of Energy under contract no. DE-AC02-06CH11357. A.G., M.D., D.G., G.R. and D.A.D.C. thank the French National Research Agency for its support through the Labex Store-EX project (ANR-10LABEX-76-01).

ACKNOWLEDGMENT

We acknowledge Diamond Light Source for time awarded to the Energy Materials BAG on Beamline B18, under Proposal sp12559. We would like to thank A.V. Chadwick and G. Cibin for assistance with the XAS measurements at Diamond Light Source.

REFERENCES

(1) Willinger, E.; Massué, C.; Schlögl, R.; Willinger, M. G. Identifying Key Structural Features of IrOx Water Splitting Catalysts. *J. Am. Chem. Soc.* **2017**, *139* (34), 12093–12101.

(2) Carmo, M.; Fritz, D. L.; Mergel, J.; Stolten, D. A Comprehensive Review on PEM Water Electrolysis. *Int. J. Hydrogen Energy* **2013**, *38* (12), 4901–4934.

(3) Vesborg, P. C. K.; Jaramillo, T. F. Addressing the Terawatt Challenge: Scalability in the Supply of Chemical Elements for Renewable Energy. *RSC Adv.* **2012**, *2* (21), 7933–7947.

(4) Kibsgaard, J.; Chorkendorff, I. Considerations for the Scaling-up of Water Splitting Catalysts. *Nat. Energy* **2019**, *4* (6), 430–433.

(5) Wei, C.; Rao, R. R.; Peng, J.; Huang, B.; Stephens, I. E. L.; Risch, M.; Xu, Z. J.; Shao-Horn, Y. Recommended Practices and Benchmark Activity for Hydrogen and Oxygen Electrocatalysis in Water Splitting and Fuel Cells. *Adv. Mater.* **2019**, *31* (31), 1806296.

(6) Bernt, M.; Siebel, A.; Gasteiger, H. A. Analysis of Voltage Losses in PEM Water Electrolyzers with Low Platinum Group Metal Loadings. *J. Electrochem. Soc.* **2018**, *165* (5), F305–F314.

(7) Zhao, Y.; Hernandez-Pagan, E. A.; Vargas-Barbosa, N. M.; Dysart, J. L.; Mallouk, T. E. A High Yield Synthesis of Ligand-Free Iridium Oxide Nanoparticles with High Electrocatalytic Activity. *J. Phys. Chem. Lett.* **2011**, *2* (5), 402–406.

(8) Yagi, M.; Tomita, E.; Kuwabara, T. Remarkably High Activity of Electrodeposited IrO_2 film for Electrocatalytic Water Oxidation. *J. Electroanal. Chem.* **2005**, *579* (1), 83–88.

(9) Gao, J.; Xu, C.; Hung, S.; Liu, W.; Cai, W.; Zeng, Z.; Jia, C.; Chen, H. M.; Xiao, H.; Li, J.; et al. Breaking Long-Range Order in Iridium Oxide by Alkali Ion For. *J. Am. Chem. Soc.* **2019**, *141*, 3014–3023.

(10) Grimaud, A.; Diaz-Morales, O.; Han, B.; Hong, W. T.; Lee, Y. L.; Giordano, L.; Stoerzinger, K. A.; Koper, M. T. M.; Shao-Horn, Y. Activating Lattice Oxygen Redox Reactions in Metal Oxides to Catalyse Oxygen Evolution. *Nat. Chem.* **2017**, *9* (5), 457–465.

(11) Seitz, L. C.; Dickens, C. F.; Nishio, K.; Hikita, Y.; Montoya, J.; Doyle, A.; Kirk, C.; Vojvodic, A.; Hwang, H. Y.; Norskov, J. K.; et al. A Highly Active and Stable $IrO_x/SrIrO_3$ Catalyst for the Oxygen Evolution Reaction. *Science (80-.).* **2016**, *353* (6303), 1011 LP – 1014.

(12) Chen, Y.; Li, H.; Wang, J.; Du, Y.; Xi, S.; Sun, Y.; Sherburne, M.; Ager, J. W.; Fisher, A. C.; Xu, Z. J. Exceptionally Active Iridium Evolved from a Pseudo-Cubic Perovskite for Oxygen Evolution in Acid. *Nat. Commun.* **2019**, *10* (1), 572.

(13) Diaz-Morales, O.; Raaijman, S.; Kortlever, R.; Kooyman, P. J.; Wezendonk, T.; Gascon, J.; Fu, W. T.; Koper, M. T. M. Iridium-Based Double Perovskites for Efficient Water Oxidation in Acid Media. *Nat. Commun.* **2016**, *7*, 12363.

(14) Zhang, R.; Dubouis, N.; Osman, M. Ben; Yin, W.; Sougrati, M. T.; Corte, D. A. D.; Giaume, D.; Grimaud, A. A Dissolution / Precipitation Equilibrium on the Surface of Iridium- Based Perovskites Controls Their Activity as Oxygen Evolution Reaction Catalysts in Acidic Media Communications Angewandte. *Angew. Chemie - Int. Ed.* **2019**, *58* (14), 4571–4575.

(15) Cherevko, S.; Geiger, S.; Kasian, O.; Kulyk, N.; Grote, J. P.; Savan, A.; Shrestha, B. R.; Merzlikin, S.; Breitbach, B.; Ludwig, A.; et al. Oxygen and Hydrogen Evolution Reactions on Ru, RuO2, Ir, and IrO2thin Film Electrodes in Acidic and Alkaline Electrolytes: A Comparative Study on Activity and Stability. *Catal. Today* **2016**, *262*, 170–180.

(16) Kim, Y.-T.; Lopes, P. P.; Park, S.-A.; Lee, A.-Y.; Lim, J.; Lee, H.; Back, S.; Jung, Y.; Danilovic, N.; Stamenkovic, V.; et al. Balancing Activity, Stability and Conductivity of Nanoporous Core-Shell Iridium/Iridium Oxide Oxygen Evolution Catalysts. *Nat. Commun.* **2017**, *8* (1), 1449.

(17) Pearce, P.; Yang, C.; Iadecola, A.; Rodriguez-Carvajal, J.; Rousse, G.; Dedryvère, R.; Abakumov, A. M.; Giaume, D.; Deschamps, M.; Tarascon, J.-M.; et al. Revealing the Reactivity of the Iridium Trioxide Intermediate for the Oxygen Evolution Reaction in Acidic Media. *Chem. Mater.* **2019**, *31* (15), 5845–5855.

(18) Zhang, R.; Pearce, P. E.; Duan, Y.; Dubouis, N.; Marchandier, T.; Grimaud, A. Importance of Water Structure and Catalyst–Electrolyte Interface on the Design of Water Splitting Catalysts. *Chem. Mater.* **2019**, *31* (20), 8248–8259.

(19) Kasian, O.; Grote, J.-P.; Geiger, S.; Cherevko, S.; Mayrhofer, K. J. J. The Common Intermediates of Oxygen Evolution and Dissolution Reactions during Water Electrolysis on Iridium. *Angew. Chemie Int. Ed.* **2018**, *57* (9), 2488–2491.

(20) Perez, A. J.; Beer, R.; Lin, Z.; Salager, E.; Taberna, P.; Abakumov, A. M.; Simon, P.; Tarascon, J. Proton Ion Exchange Reaction in Li_3IrO_4 : A Way to New $H_{3+x}IrO_4$ Phases

Electrochemically Active in Both Aqueous and Nonaqueous Electrolytes. *Adv. Energy Mater.* **2018**, *8* (13), 1702855.

(21) Chen, Y.; Li, H.; Wang, J.; Du, Y.; Xi, S.; Sun, Y.; Sherburne, M.; Ager, J. W.; Fisher, A. C.; Xu, Z. J. Exceptionally Active Iridium Evolved from a Pseudo-Cubic Perovskite for Oxygen Evolution in Acid. *Nat. Commun.* **2019**, *10* (1), 572.

(22) Geiger, S.; Kasian, O.; Ledendecker, M.; Pizzutilo, E.; Mingers, A. M.; Fu, W. T.; Diaz-Morales, O.; Li, Z.; Oellers, T.; Fruchter, L.; et al. The Stability Number as a Metric for Electrocatalyst Stability Benchmarking. *Nat. Catal.* **2018**, *1* (7), 508–515.

(23) Gatimu, A. J.; Berthelot, R.; Muir, S.; Sleight, A. W.; Subramanian, M. A. Synthesis and Characterization of $Sr_2Ir_{1-x}M_xO_4$(M=Ti, Fe, Co) Solid Solutions. *J. Solid State Chem.* **2012**, *190*, 257–263.

(24) Qasim, I.; Kennedy, B. J.; Avdeev, M. Synthesis, Structures and Properties of Transition Metal Doped $SrIrO_3$. *J. Mater. Chem. A* **2013**, *1* (9), 3127–3132.

(25) Messinger, R. J.; Ménétrier, M.; Salager, E.; Boulineau, A.; Duttine, M.; Carlier, D.; Ateba Mba, J.-M.; Croguennec, L.; Masquelier, C.; Massiot, D.; et al. Revealing Defects in Crystalline Lithium-Ion Battery Electrodes by Solid-State NMR: Applications to LiVPO4F. *Chem. Mater.* **2015**, *27* (15), 5212–5221.

(26) Bastow, T. J.; Hodge, R. M.; Hill, A. J. 1H and 13C NMR Studies of Water and Heavy Water Absorption in Poly(Vinyl Alcohol) Hydrogels. *J. Memb. Sci.* **1997**, *131* (1), 207–215.

(27) Eckert, H.; Yesinowski, J. P.; Silver, L. A.; Stolper, E. M. Water in Silicate Glasses: Quantitation and Structural Studies by Proton Solid Echo and Magic Angle Spinning NMR Methods. *J. Phys. Chem.* **1988**, *92* (7), 2055–2064.

(28) Jorgensen, J. D.; Dabrowski, B.; Pei, S.; Richards, D. R.; Hinks, D. G. Structure of the Interstitial Oxygen Defect in La_2NiO_4. *Phys. Rev. B* **1989**, *40* (4), 2187–2199.

(29) Girgsdies, F.; Schöllhorn, R. Spontaneous Topotactic Oxidation of La_2CoO_4 at Room Temperature. *Solid State Commun.* **1994**, *91* (2), 111–112.

(30) Weber, D.; Schoop, L. M.; Wurmbrand, D.; Nuss, J.; Seibel, E. M.; Tafti, F. F.; Ji, H.; Cava, R. J.; Dinnebier, R. E.; Lotsch, B. V. Trivalent Iridium Oxides: Layered Triangular Lattice Iridate K0.75Na0.25IrO2 and Oxyhydroxide IrOOH. *Chem. Mater.* **2017**, *29* (19), 8338–8345.

(31) Lee, K.; Osada, M.; Hwang, H. Y.; Hikita, Y. Oxygen Evolution Reaction Activity in $IrO_x/SrIrO_3$ Catalysts: Correlations between Structural Parameters and the Catalytic Activity. *J. Phys. Chem. Lett.* **2019**, *10* (7), 1516–1522.

(32) Tang, R.; Nie, Y.; Kawasaki, J. K.; Kuo, D.-Y.; Petretto, G.; Hautier, G.; Rignanese, G.-M.; Shen, K. M.; Schlom, D. G.; Suntivich, J. Oxygen Evolution Reaction Electrocatalysis on SrIrO3 Grown Using Molecular Beam Epitaxy. *J. Mater. Chem. A* **2016**, *4* (18), 6831–6836.

(33) Xu, K.; Song, F.; Gu, J.; Xu, X.; Liu, Z.; Hu, X. Solvent-Induced Surface Hydroxylation of a Layered Perovskite $Sr_3FeCoO_{7-\delta}$ for Enhanced Oxygen Evolution Catalysis. *J. Mater. Chem. A* **2018**, *6* (29), 14240–14245.

(34) Man, I.C. Theoretical study of electro-catalysts for oxygen evolution. Kgs. Lyngby, denmark: Technical University of Denmark, **2011**.

(35) Escudero-Escribano, M.; Pederson, A.F.; Paoli, E.A.; Frydendal, R.; Friebel, D.; Malacrida, P.; Rossmeisl, J.; Stephens, I.E.L.; Chorkendorff, I. Importance of surface IrO_x in stabilizing RuO_2 for oxygen evolution. *J. Phys. Chem. B* **2018**, *122* (2), 947–955.

(36) Blakemore, J. D.; Schley, N. D.; Kushner-Lenhoff, M. N.; Winter, A. M.; D'Souza, F.; Crabtree, R. H.; Brudvig, G. W. Comparison of Amorphous Iridium Water-Oxidation Electrocatalysts Prepared from Soluble Precursors. *Inorg. Chem.* **2012**, *51* (14), 7749–7763.

(37) Grimaud, A.; May, K. J.; Carlton, C. E.; Lee, Y.-L.; Risch, M.; Hong, W. T.; Zhou, J.; Shao-Horn, Y. Double Perovskites as a Family of Highly Active Catalysts for Oxygen Evolution in Alkaline Solution. *Nat. Commun.* **2013**, *4*, 2439.

(38) Pfeifer, V.; Jones, T. E.; Velasco Vélez, J. J.; Massué, C.; Greiner, M. T.; Arrigo, R.; Teschner, D.; Girgsdies, F.; Scherzer, M.; Allan, J.; et al. The Electronic Structure of Iridium Oxide Electrodes Active in Water Splitting. *Phys. Chem. Chem. Phys.* **2016**, *18* (4), 2292–2296.

(39) Takimoto, D.; Fukuda, K.; Miyasaka, S.; Ishida, T.; Ayato, Y.; Mochizuki, D.; Shimizu, W.; Sugimoto, W. Synthesis and Oxygen Electrocatalysis of Iridium Oxide Nanosheets. *Electrocatalysis* **2017**, *8* (2), 144–150.

(40) Laha, S.; Lee, Y.; Podjaski, F.; Weber, D.; Duppel, V.; Schoop, L. M.; Pielnhofer, F.; Scheurer, C.; Müller, K.; Starke, U.; et al. Ruthenium Oxide Nanosheets for Enhanced Oxygen Evolution Catalysis in Acidic Medium. *Adv. Energy Mater.* **2019**, *9* (15), 1803795.

(41) Nong, H. N.; Reier, T.; Oh, H.-S.; Gliech, M.; Paciok, P.; Vu, T. H. T.; Teschner, D.; Heggen, M.; Petkov, V.; Schlögl, R.; et al. A Unique Oxygen Ligand Environment Facilitates Water Oxidation in Hole-Doped $IrNiO_x$ Core–Shell Electrocatalysts. *Nat. Catal.* **2018**, *1* (11), 841–851.

(42) Weber, D.; Schoop, L. M.; Wurmbrand, D.; Laha, S.; Podjaski, F.; Duppel, V.; Müller, K.; Starke, U.; Lotsch, B. V. IrOOH Nanosheets as Acid Stable Electrocatalysts for the Oxygen Evolution Reaction. *J. Mater. Chem. A* **2018**, *6* (43), 21558–21566.

(43) Lee, Y.; Suntivich, J.; May, K. J.; Perry, E. E.; Shao-Horn, Y. Synthesis and Activities of Rutile IrO_2 and RuO_2 Nanoparticles for Oxygen Evolution in Acid and Alkaline Solutions. *J. Phys. Chem. Lett.* **2012**, *3* (3), 399–404.

(44) Lettenmeier, P.; Majchel, J.; Wang, L.; Saveleva, V. A.; Zafeiratos, S.; Savinova, E. R.; Gallet, J.-J.; Bournel, F.; Gago, A. S.; Friedrich, K. A. Highly Active Nano-Sized Iridium Catalysts: Synthesis and Operando Spectroscopy in a Proton Exchange Membrane Electrolyzer. *Chem. Sci.* **2018**, *9* (14), 3570–3579.

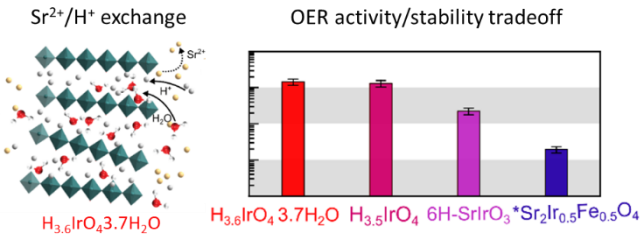

Table of Contents Graphic